nanomaterials

MDPI

Article

Zero-Dimensional Tellurium-Based Organic–Inorganic Hybrid Halide Single Crystal with Yellow-Orange Emission from Self-Trapped Excitons

Xiangyan Yun [1,2], Jingheng Nie [3], Hanlin Hu [4], Haizhe Zhong [2], Denghui Xu [1,*], Yumeng Shi [5,*] and Henan Li [5]

[1] Department of Physics, Beijing Technology and Business University, Beijing 100048, China
[2] International Collaborative Laboratory of 2D Materials for Optoelectronics Science and Technology of Ministry of Education, Institute of Microscale Optoelectronics, Shenzhen University, Shenzhen 518060, China
[3] Guangdong Rare Earth Photofunctional Materials Engineering Technology Research Center, School of Chemistry and Environment, Jiaying University, Meizhou 514015, China
[4] Hoffman Institute of Advanced Materials, Shenzhen Polytechnic, Shenzhen 518060, China
[5] School of Electronics and Information Engineering, Shenzhen University, Shenzhen 518060, China; henan.li@szu.edu.cn
* Correspondence: xudh@btbu.edu.cn (D.X.); yumeng.shi@szu.edu.cn (Y.S.)

Abstract: Organic–inorganic hybrid halides and their analogs that exhibit efficient broadband emission from self-trapped excitons (STEs) offers an unique pathway towards realization of highly efficient white light sources for lighting applications. An appropriate dilution of ns^2 ions into a halide host is essential to produce auxiliary emissions. However, the realization of ns^2 cation-based halides phosphor that can be excited by blue light-emitting diode (LED) is still rarely reported. In this study, a zero-dimensional Te-based single crystal $(C_8H_{20}N)_2TeCl_6$ was synthesized, which exhibits a yellow-orange emission centered at 600 nm with a full width at half maximum of 130 nm upon excitation under 437 nm. Intense electron–phonon coupling was confirmed in the $(C_8H_{20}N)_2TeCl_6$ single crystal and the light emitting mechanism is comprehensively discussed. The results of this study are pertinent to the emissive mechanism of Te-based hybrid halides and can facilitate discovery of unidentified metal halides with broadband excitation features.

Keywords: Te-based; low dimensional; single crystal; hybrid halide; self-trapped exciton

Citation: Yun, X.; Nie, J.; Hu, H.; Zhong, H.; Xu, D.; Shi, Y.; Li, H. Zero-Dimensional Tellurium-Based Organic–Inorganic Hybrid Halide Single Crystal with Yellow-Orange Emission from Self-Trapped Excitons. *Nanomaterials* **2024**, *14*, 46. https://doi.org/10.3390/nano14010046

Academic Editor: Myungkwan Song

Received: 18 November 2023
Revised: 19 December 2023
Accepted: 21 December 2023
Published: 22 December 2023

1. Introduction

Lead-free perovskite materials—which exhibit strong photoelectric conversion efficiency, exceptional photoluminescence quantum yield (PLQY), high light absorption coefficients, and excellent flexibility—are an active area of research in flexible displays, semiconductor high-energy lasers, X-ray scintillator, light-emitting diodes, and infrared detectors [1–4]. The general structural formula of perovskites has progressively developed from the primary $AB(II)X_3$ to $A_2B(I)B(III)X_6$ (halide double perovskites), $A_2B(IV)X_6$ (vacancy-ordered perovskites), $A_3B(III)2X_9$ (halide triple perovskites), $A_4B(II)B(III)_2X_{12}$ (halide quadruple perovskites) and other configurations [5–7]. A is monovalent organic or inorganic cations, such as $CH_3NH_3^+$, $NH_2CHNH_2^+$, Cs^+, Rb^+, K^+; B(I), B(II), B(III) and B(IV), respectively, stand for metal cations with different valence states, such as Ag^+, Cu^+, Sn^{2+}, Zn^{2+}, Sb^{3+}, In^{3+}, Zr^{4+}, Hf^{4+}, Te^{4+}, and Sn^{4+}; X represents monovalent halide anion, such as Cl^-, I^-, Br^- or mixed halide anions [8,9]. Moreover, perovskites and perovskite derivatives can be classified into three-, two-, one-, and zero-dimensional (0D) at the molecular level [10]. Low-dimensional metal halide materials have large forbidden bands and high exciton binding energies, because of their remarkable crystal and electronic structures [11,12]. Introducing organic molecules leads to extraordinary possibilities in

structure and performance research of metal halides with various dimensions [13]. Therefore, developing organic–inorganic hybrid, lead-free, low-dimensional metal halides is important for expanding functional applications.

Presently, the exceptional photoelectric performance of organic–inorganic hybrid, lead-free, low-dimensional metal halides is particularly influenced by B-site metal cations [14]. Metal cations containing the outermost electron arrangement as ns^2 lone pair electrons are called ns^2 ions. $5S^2$ ions (Sn^{2+}, Sb^{3+}, Te^{4+}) and $6S^2$ ions (Bi^{3+}, Pb^{2+}) can exhibit their lone pair electron transition characteristics during photoexcitation. Metal halide materials containing ns^2 cations have advantages compared with analogous materials that contain other cations, in terms of outstanding self-trapped exciton (STE) emission and other optoelectronic characteristics [15–18]. For example, the Zhao group reported that $(C_{10}H_{22}N)_2SbBr_5$ and $(C_{10}H_{22}N)_3Sb_2Br_9$ exhibit orange emission with maxima at 640 and 660 nm, respectively, which originates from STE emission of the Sb^{3+} cation [19]. Nevertheless, currently, the widely investigated Sb-based halides cannot be excited with blue light, which also occurs in, e.g., Bi- or Ge-based halides [20,21]. Mn-based halides can be excited with blue light; however, the luminescence mechanism of Mn-based halides is attributable to the *d-d* transition of Mn ions, which leads to their lack of bright STE broad-spectrum emission [22–24]. In that vein, an immense challenge in STE emitters is finding an STE emitter with ultra-broadband excitation involving blue light regions.

Significantly, tetravalent tellurium ion with a lone-pair $5s^2$ electronic configuration was found to be an ion accompanied by distinctive STE emission. And the ultra-wide absorption band present in Te-based or Te-doped metal halides may cause them to be excited by blue light [25]. Recently, some progress has been achieved in all-inorganic metal halides-doped Te^{4+} ions with STE emission that can be excited by blue light. For example, Zhang et al. attributed the luminescence of Te^{4+}-doped Rb_2SnCl_6 that can be excited by blue light to the STE emission of the $[TeCl_6]^{2-}$ octahedron [26]. Li et al. developed 0D Sc(III)-based Te^{4+}-doped $Rb_2ScCl_5{\cdot}H_2O$ single crystals with a broadband orange STE emission (650 nm) that can be excited by light in the range of 240 nm to 440 nm [27]. Compared with inorganic metal halides doped with Te^{4+} ions, the STE emission research on Te-based organic–inorganic hybrid metal halides usually show limited light emission efficiency. For instance, Mirochnik et al. discovered the broadband emission of $((CH_3)_4N)_2TeCl_6$ halide at 77 K, with poor luminescence at room temperature [28]. For the time being, there are few Te-based organic–inorganic hybrid metal halides that can exhibit obvious STE emission at room temperature, although some Te-based halides can exhibit relatively high luminescence intensity at low temperatures. Therefore, there is an urgent need for new low-dimensional Te-based metal halides that exhibit STE emission at room temperature.

Inspired by the low dimensionality and configuration of metal halides, the authors of this paper designed and synthesized an organic–inorganic hybrid, lead-free, 0D $(C_8H_{20}N)_2TeCl_6$ single crystal. The structural details, optical and decay lifetime characteristics at room temperature, as well as temperature-dependent luminescence of this single crystal are discussed in detail. At room temperature, $(C_8H_{20}N)_2TeCl_6$ single crystals exhibit a broadband STE emission (λ_{em} = 600 nm) with a full width at half maximum (FWHM) of 130 nm under 437 nm excitation. Temperature-dependent data also demonstrate that the yellow-orange emission is attributable to archetypal STE emission.

2. Experimental Section

2.1. Materials

Tetraethylammonium chloride ($C_8H_{20}NCl$, 98%, Aladdin, Shanghai, China), tellurium tetrachloride ($TeCl_4$, 99%, Meryer, Shanghai, China), anhydrous ethanol (C_2H_6O, AR, Macklin, Shanghai, China), diethyl ether ($C_4H_{10}O$, AR, Sinopharm Chemical Reagent Co., Ltd., Shanghai, China) and hydrochloric acid (HCl, Sigma-Aldrich, Shanghai, China) were used as received. During the process of synthesizing $(C_8H_{20}N)_2TeCl_6$ single crystal, $TeCl_4$ materials can also be replaced with tellurium dioxide (TeO_2, 99.99%, Bide Pharmatech Co., Ltd., Shanghai, China).

2.2. Synthesis of $(C_8H_{20}N)_2TeCl_6$ Single Crystal

Anti-solvent evaporation and traditional solvothermal methods can be used to synthesize single crystals. Regarding the traditional solvothermal method, the solvent is HCl. $C_8H_{20}NCl$ (0.6628 g), $TeCl_4$ (0.5388 g) and 16 mL hydrochloric acid were loaded into a 25 mL tetrafluoroethylene reactor, heated at 120 °C for 8 h, and cooled to room temperature within 16 h. Figure S1A shows the schematic process of synthesizing $(C_8H_{20}N)_2TeCl_6$ single crystals using solvothermal method. It is worth noting that after the reaction completes, yellowish-green single crystals can be obtained in the hydrochloric acid liquid. Then, the prepared single crystals are transferred from the tetrafluoroethylene reactor to a culture dish. In order to remove the hydrochloric acid attached to the surface of the $(C_8H_{20}N)_2TeCl_6$ single crystals, an appropriate amount of anhydrous ethanol was added to the culture dish to rinse the prepared single crystals. The above flushing process is repeated for at least three times. Finally, the anhydrous ethanol in this culture dish was removed by a dropper and placed in an oven at 65 °C for 20 min of drying treatment. In addition, this experimental process can also replace 0.5388 g of $TeCl_4$ with 0.3192 g of TeO_2, while keeping most of the remaining experimental requirements unchanged. When washing $(C_8H_{20}N)_2TeCl_6$ single crystals prepared using TeO_2 as raw material, it is necessary to replace anhydrous ethanol with isopropanol. However, it should be noted that the single crystal luminescence performance synthesized using $TeCl_4$ is superior to that synthesized using TeO_2. The luminescence characteristics detected in this article are the properties of single crystals prepared using $TeCl_4$. Regarding anti-solvent evaporation, first, 0.002 mol $C_8H_{20}NCl$ (0.3314 g) and 0.001 mol $TeCl_4$ (0.2694 g) were dissolved in a single solvent (1.5 mL C_2H_6O at 65 °C) to form a clear precursor solution (Figure S1B). Then, the as-formed precursor solution was transferred to an unsealed 10 mL glass bottle, the mouth of this 10 mL glass bottle was sealed with plastic film, and sharp needles were used to puncture several breathable openings. Finally, this small glass bottle was placed into a large sealed weighing bottle with diethyl ether reagent at the bottom. Within 3 d at room temperature, the yellowish-green crystals formed. The $(C_8H_{20}N)_2TeCl_6$ single crystals synthesized by the anti-solvent evaporation method were washed with anhydrous ethanol. The drying conditions were consistent with those used in the traditional solvothermal method above.

2.3. Characterization

Powder XRD measurements of $(C_8H_{20}N)_2TeCl_6$ powder were conducted using an X-ray diffractometer (D2 Phaser) with Cu-Kα radiation (λ = 1.5418 Å, 40 kV, 20 mA). The data used for Powder XRD analysis (2θ range 5–60°) was collected in a step-scanning mode with a step size of 0.02° and 0.5 s counting time per step. The single crystal XRD measurements were performed with a Bruker D8 Venture diffractometer. $(C_8H_{20}N)_2TeCl_6$ crystals were maintained at 193.15 K during data collection. In Olex2, the structure was solved with the olex2.solve structure solution program using charge-flipping, and refined with the XL refinement package using least-squares minimization [29–31]. The absorption spectra were collected using a UV-3600i Plus UV–visible–NIR spectrophotometer (Shimadzu, Kyoto, Japan), in which $BaSO_4$ commercial backing plate was used as the reference standard. The photoluminescence excitation (PLE) and photoluminescence (PL) patterns were recorded with FLUOROMAX_PLUS fluorescence spectrometer (HORIBA Scientific, Kyoto, Japan). The correlated color temperature (CCT) and color purity of $(C_8H_{20}N)_2TeCl_6$ powder were calculated using ColorCalculator v7.77 software. The color purity was calculated based on $Color\ purity = \sqrt{\frac{(x_r-x_i)^2+(y_r-y_i)^2}{(x_m-x_i)^2+(y_m-y_i)^2}} \times 100\%$ equation, in which (x_i, y_i) was the standard white light coordinate, (x_m, y_m) represented the Commission Internationale de I'Eclairage (CIE) coordinate of the dominant wavelength, and (x_r, y_r) was the CIE coordinate of $(C_8H_{20}N)_2TeCl_6$ halide. The PLQY pattern was recorded with an FS5 spectrofluorometer (Edinburgh integrated steady-state transient fluorescence spectrometer) at room temperature. The decay lifetimes were measured using an FS5 instrument equipped with a 405 nm

(Edinburgh Instruments, Livingston, Scotland, UK; EPL-405 picosecond pulsed diode laser, 5 mW) laser.

The time width of the 405 nm laser used for the dynamics of emission decays was 5 µs window, and the single-photon counting capability was 5000 counts (1024 channels). Temperature-dependent PL spectroscopic measurements were conducted using an FS5 equipped with a temperature precision controller and liquid nitrogen input equipment (Beijing Physike Technology Co., Ltd., Beijing, China).

3. Results and Discussion

As-grown $(C_8H_{20}N)_2TeCl_6$ single crystals were synthesized using the traditional solvothermal method, and single crystal X-ray diffraction (SCXRD) was used to confirm its structure. The crystal structure of $(C_8H_{20}N)_2TeCl_6$ exhibited a monoclinic space group $P2_1/c$; the cell parameters were a = 14.0511 Å, b = 14.6234(15) Å, c = 13.0285(15) Å, and V = 2677.0(5) Å^3. The crystallographic information file (CIF) of $(C_8H_{20}N)_2TeCl_6$ single crystal has been uploaded to the Cambridge Crystallographic Data Centre (CCDC#2304048). Furthermore, Tables S1–S7 (Supporting Information) show the remaining essential crystallographic data as well as relevant parameter analysis, respectively. As shown in Figure 1A, $(C_8H_{20}N)_2TeCl_6$ exhibited a 0D structure with units of $[TeCl_6]^{2-}$ octahedral, and each isolated $[TeCl_6]^{2-}$ octahedron was surrounded by extensive organic molecular $(C_8H_{20}N)^+$ units [32,33]. Figure 1B shows that each $[TeCl_6]^{2-}$ octahedron contains two Te-Cl bond distances (2.5346 Å and 2.5564 Å) and two Cl-Te-Cl bond angles (89.371° and 90.629°). From the same perspective, the phenomenon of two $[TeCl_6]^{2-}$ octahedra twisting in opposite directions can be observed (Figure 1C). The simulated SCXRD pattern of $(C_8H_{20}N)_2TeCl_6$ is highly consistent with the powder XRD pattern (Figure 1D), which indicates that the powder prepared by grinding exhibited an identical structure as the single crystal [34]. Figure S2 shows a locally enlarged XRD pattern, which also demonstrates good consistency between the experimental data and the calculated data.

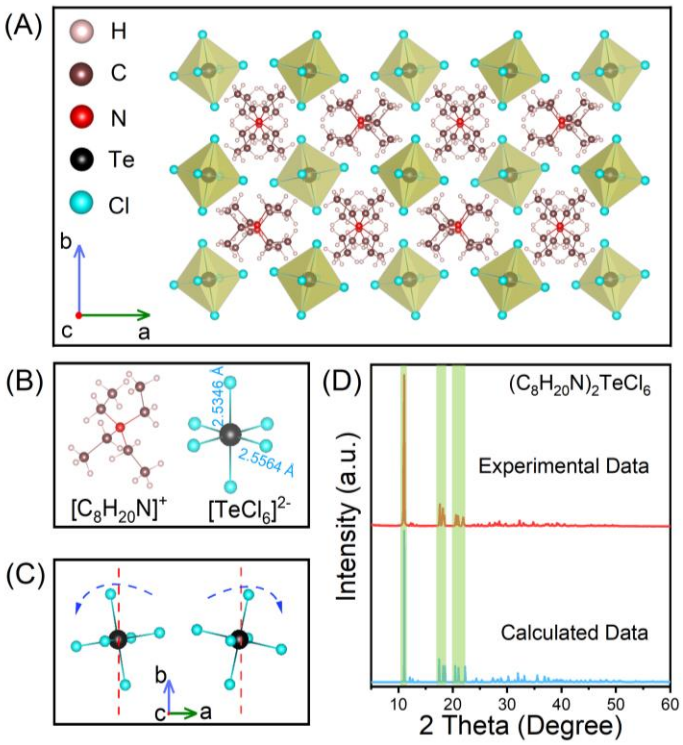

Figure 1. (**A**) Structural diagram of $(C_8H_{20}N)_2TeCl_6$ single crystals. (**B**) The structure of the individual $[C_8H_{20}N]^+$ and $[TeCl_6]^{2-}$. (**C**) $[TeCl_6]^{2-}$ octahedral distortion diagram. (**D**) XRD pattern of $(C_8H_{20}N)_2TeCl_6$.

Regarding Pb-free metal halide luminescent systems, the luminescent behavior of ns^2 metal ions as visible and near-infrared (NIR) luminescent centers is an active area of research. Te^{4+}, Sb^{3+}, Sn^{2+} and Bi^{3+} ions exhibit analogous chemical properties and electronic configurations as significant ions [15,35]. The Te^{4+} ion containing $5s^2$ lone pair electrons has a similar ground state electronic structure to the Sb^{3+} ion that has been extensively studied in the field of metal halide luminescence. Figure S3A shows a schematic of the excitation state of Te^{4+} in metal halides. The excited states (sp) split into two branches ($^1P_1$ and ^3P_n) under the influence of spin–orbit coupling (SOC); the excited-state splitting phenomena of $^1P_1$ and $^3P_1$ follows the order of energy from low to high, which is usually attributed to the lattice symmetry breaking caused by the Jahn–Teller effect [36]. Several previously reported papers (Cs_2SnCl_6:Te^{4+}; Cs_2ZrCl_6:Te^{4+}) have confirmed the level ($^1P_1$ and $^3P_1$) splitting phenomenon of Te^{4+} ions [37,38]. $^1S_0$–$^1P_1$, $^1S_0$–$^3P_2$, and $^1S_0$–$^3P_1$ transitions are allowed, vibration-induced, and spin–orbit-allowed, respectively. The spin–orbit-allowed behavior can derive from the intense effect of SOC by tellurium atoms [38,39]. Deformation of octahedra is common in $[TeCl_6]^{2-}$ octahedra that are susceptible to the Jahn–Teller effect (Figure S3B). The vibrational mode of $[TeCl_6]^{2-}$ octahedra in $(C_8H_{20}N)_2TeCl_6$ belongs to $v2$ mode [35].

Figure 2A shows the UV–visible absorption spectrum of $(C_8H_{20}N)_2TeCl_6$ halide. The absorption curve of $(C_8H_{20}N)_2TeCl_6$ halide exhibits an ultra-wide absorption band in the wavelength range of 200–500 nm, which is similar to reports for $(C_{13}H_{22}N)_2TeCl_6$ and $(C_{20}H_{20}N)_2TeCl_6$ [40,41]. The ultrabroad absorption bands are attributable to the dipole-allowed, vibration-allowed, and spin–orbit-allowed transitions of Te^{4+} ions. And the inset shows the optical images of $(C_8H_{20}N)_2TeCl_6$ under the illumination of daylight and 365 nm UV light. $(C_8H_{20}N)_2TeCl_6$ single crystal appears yellowish-green and transparent in daylight; however, when exposed to UV light at 365-nm, it displays yellow-orange fluorescence. In addition, the same emission occurs in the $(C_8H_{20}N)_2TeCl_6$ powder. Figure 2B shows the normalized room-temperature PL emission and excitation spectra of $(C_8H_{20}N)_2TeCl_6$. The PLE spectrum (monitored at 600 nm) consists of an ultrabroad band in the UV and blue regions with a peak at 437 nm, indicating that this halide could be excited with available blue light-emitting diode chips. Upon excitation at 437 nm, $(C_8H_{20}N)_2TeCl_6$ exhibited a strong-broad yellow-orange emission ranging from 450 to 800 nm, with a FWHM of 130 nm and a peak at 600 nm. In addition, there was a large Stokes shift of 163 nm. Figure 2C shows the pseudo-color map of a PL/PLE of $(C_8H_{20}N)_2TeCl_6$ sample at room temperature, in which the characteristics of emission spectra under variable excitation and STE emission characteristics of Te^{4+} ions can have a precise correspondence [42]. To gain a deeper understanding of the luminous mechanism in the $(C_8H_{20}N)_2TeCl_6$ system, further information is obtained from wavelength-scanning time-correlated decay experiments. Under 405 nm laser excitation, the lifetime monitored at 600 nm in $(C_8H_{20}N)_2TeCl_6$ can be fitted using a single exponential equation: $I = Ae^{-t/\tau}$, in which I is the PL intensity, A refers to the constant, and τ represents the fitting decay time. The fitting lifetime of $(C_8H_{20}N)_2TeCl_6$ halide was 236.43 ns, and the value of R^2 (R^2 = 0.999) indicates that this fitting is reliable (Figure 2D). The decay-mapping and fitting results are shown in Figure 2E and Table S8 (Supporting Information). The emission peaks located from 540 nm to 660 nm represent similar fitting lifetimes, indicating that there was only one PL component. The multiple lifetimes fitted by $(C_8H_{20}N)_2TeCl_6$ sample are similar to the previously reported lifetime characteristics of STE luminescence behavior related to Te^{4+} ion doping (Rb_2ZrCl_6:Te^{4+}, 235.62 ns; Cs_2ZnCl_4:Te^{4+}, 53.2 ns) or Te-based materials ($(Ph_3S)_2TeCl_6$, 42.7 ns) [35,42,43]. The lifetimes of hundreds of nanoseconds are attributable to STE emission of $[TeCl_6]^{2-}$ octahedrons. The CIE coordinate of $(C_8H_{20}N)_2TeCl_6$ halide is (0.52, 0.46) with a CCT of 2376 K and a color purity of 95.2% (Figure 2F), which is higher than that of Cs_2SnCl_6:Te^{4+} (84.69%) [44]. Regarding Te-based halides, a constraint is that the PLQY at room temperature is low, which can cause STE luminescence emission that is insubstantial to the unaided eye. Here, the PLQY at room temperature was 10.12% (Figure S4).

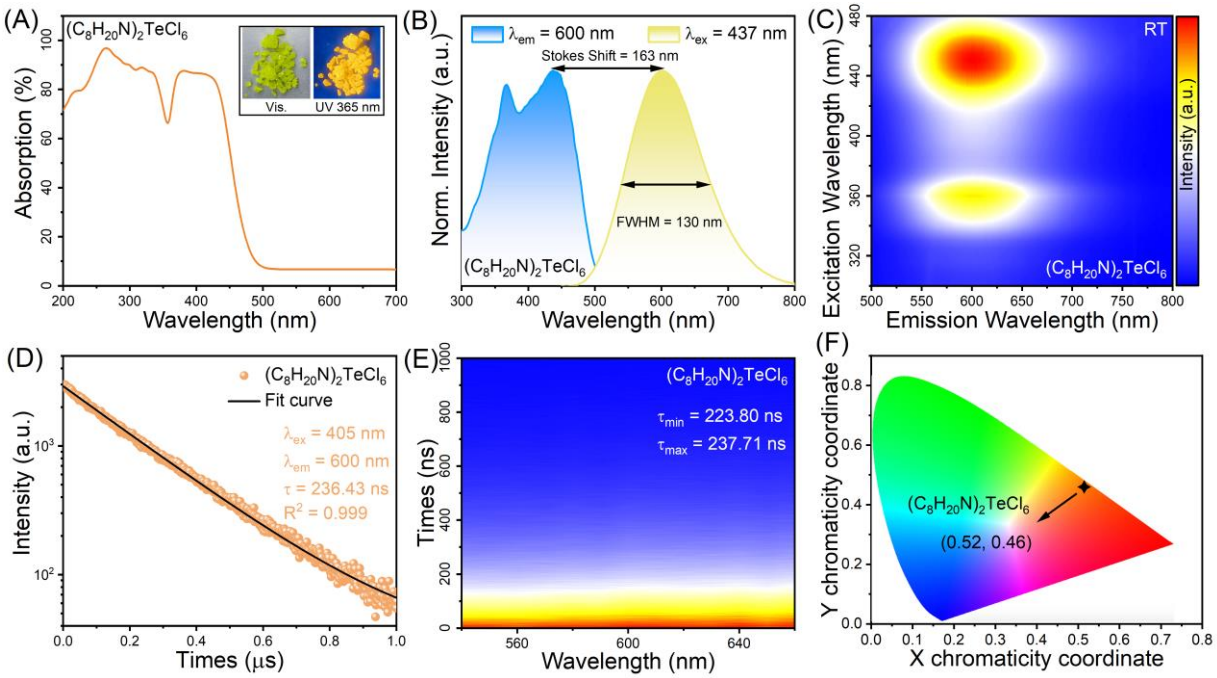

Figure 2. (**A**) Absorption spectra of $(C_8H_{20}N)_2TeCl_6$. The inset shows the optical images of $(C_8H_{20}N)_2TeCl_6$ under the illumination of daylight and 365 nm UV light. (**B**) PLE and PL spectra of $(C_8H_{20}N)_2TeCl_6$ at RT. (**C**) Pseudo color map of PL/PLE of $(C_8H_{20}N)_2TeCl_6$. (**D**) Emission wavelength scanning decay of $(C_8H_{20}N)_2TeCl_6$ excited by 405 nm. (**E**) Emission wavelength scanning decay of $(C_8H_{20}N)_2TeCl_6$ excited by 405 nm. (**F**) CIE color coordinate of $(C_8H_{20}N)_2TeCl_6$ sample.

To obtain deep insights into the mechanism of STE emission of Te-based halides, temperature-dependent PL spectroscopic measurements of $(C_8H_{20}N)_2TeCl_6$ halide were implemented in the range of 90 K to 300 K. Figure 3A shows the temperature-dependent PL spectra of $(C_8H_{20}N)_2TeCl_6$. The test temperature was negatively correlated with the PL intensity. As the test temperature continued to increase from cryogenic to room temperature, an inconspicuous blue shift of the emission band was observed, which originates from electron–phonon coupling interactions and thermal expansion of the metal halide lattice [45]. According to the currently recognized theory of STE luminescence in metal halides, the STE emissions are affected by the strength of exciton–phonon coupling. Figure 3B shows a plot of the FWHM (obtained using Gaussian fitting) and integrated PL intensity against the temperature. Conventional theories use the Huang–Rhys factor (S), dimensionless, to characterize the strength of electron–phonon coupling, which exhibits a close correlation with the FWHM. The Huang–Rhys factor can be calculated using the fitting formula [46]:

$$\mathrm{FWHM} = 2.36\sqrt{S}\hbar\omega_{phonon}\sqrt{coth\frac{\hbar\omega_{phonon}}{2k_BT}} \quad (1)$$

where $\hbar\omega_{phonon}$, T, and k_B represent the phonon frequency, practical temperature, and the Boltzmann constant, respectively. Through multiple derivations and simplifications of Formula (1), Figure 3C shows the functional relationship between FWHM^2 vs. $2kT$ as well as the linear fitting line (red line). Regarding the $(C_8H_{20}N)_2TeCl_6$ halide, the phonon frequency and Huang–Rhys factor were ca. 0.01303 eV, and 38.71, respectively. In general, there is a certain correlation between the S value and the ease of STE formation. For STE emissions of metal halides, the appropriate value of S is generally between 10 and 40 [47]. For instance, pure inorganic Sb^{3+}-doped Rb_4CdCl_6 sample with typical STE emission has an S of 34.94, which is extremely similar to the 38.71 of $(C_8H_{20}N)_2TeCl_6$ halide [48]. The Huang–Rhys factor of $(C_8H_{20}N)_2TeCl_6$ halide is evidently higher than the previously reported halides of $Cs_2Sn_{0.89}Te_{0.11}Cl_6$ (16.0), $(CH_3CH_2CH_2)_4NCuCl_2$ (16.4),

and Sb^{3+}-doped $Cs_3Cd_2Cl_7$ (30.06) with emblematic STE emissions, indicative of intense exciton–phonon coupling and Jahn–Teller distortion in $(C_8H_{20}N)_2TeCl_6$ [48–50]. Moreover, according to the STE emission calculation formula ($E_{PL} = E_g - E_b - E_{STE} - E_d$), the exciton binding energy (E_b) is a pertinent physical parameter that is used to deduce STE emission. Figure 3D shows the temperature-dependent integrated PL intensity; the E_b values were determined using the Arrhenius expression:

$$I(T) = I_0 / \left(1 + Aexp^{-E_b/k_BT}\right) \quad (2)$$

where $I(T)$ and I_0 represent the integrated intensity at the actual measurement temperature and the integrated intensity at 0 K, respectively. The E_b of $(C_8H_{20}N)_2TeCl_6$ was ca. 338.27 meV, which is comparable with the previously reported all-inorganic low-dimensional metal halides of $Rb_2ScCl_5{\cdot}H_2O{:}Te^{4+}$ (384 meV), and $CsCu_2I_3$ (346 meV) [27]. The fitted exciton binding energy and Huang–Rhys factor can both prove that this yellow-orange broadband emission at 600 nm in $(C_8H_{20}N)_2TeCl_6$ halide is attributed to STEs of $[TeCl_6]^{2-}$ octahedral [36,37]. Overall, the luminescence mechanism for $(C_8H_{20}N)_2TeCl_6$ halide (Figure 4A) can be summarized as follows: UV or blue-light excitation leads to the electron excitation from the $^1S_0$ state to the excited states of Te–Cl. Then, the free carriers (FCs) become free excitons (FEs) through coulombic interactions. In addition, the low-dimensional (0D) structure of the $(C_8H_{20}N)_2TeCl_6$ halide is beneficial for promoting the presence of a soft lattice in this single crystal, thus easily forming STE emission. FEs are subjected to intense exciton–phonon interactions, resulting in lattice distortion of the $[TeCl_6]^{2-}$ octahedral and trapping in the STE state. Therefore, FEs ultimately fall into the newly formed STE state, leading to yellow-orange STE emission. Moreover, as shown in Figure 4B, the PXRD peak pattern of the $(C_8H_{20}N)_2TeCl_6$ sample under long-term air exposure conditions exhibit significant consistency, with several major PXRD peaks corresponding to each other in the highlighted yellow area. And the PL intensity of the $(C_8H_{20}N)_2TeCl_6$ powder after continuous exposure to 437 nm blue light for 70 h is not significantly different from the original PL intensity (Figure 4C). Hence, the above XRD and spectral results indicate that the as-synthesized $(C_8H_{20}N)_2TeCl_6$ samples have a reliable stability.

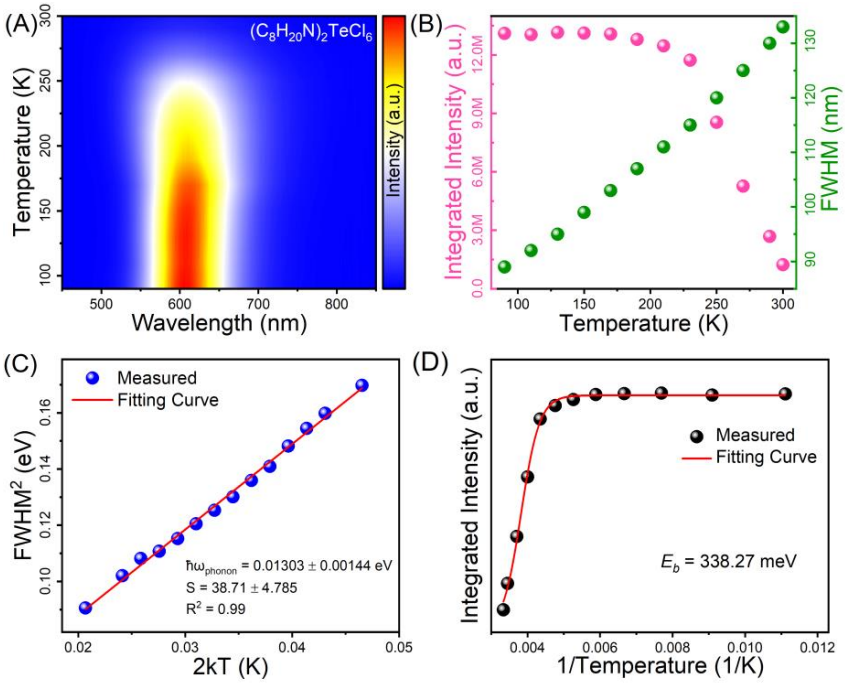

Figure 3. (**A**) Temperature-dependent PL spectrum of $(C_8H_{20}N)_2TeCl_6$. (**B**) Integrated intensity and FWHM as functions of temperature. (**C**) $FWHM^2$ as functions of 2 kT. (**D**) Integrated PL intensity as functions of 1/T.

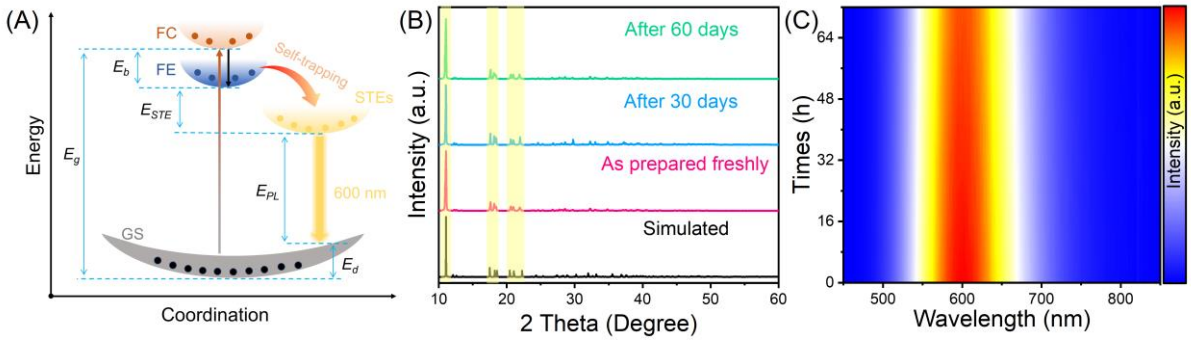

Figure 4. (**A**) Configuration coordinate diagram demonstrating the photophysical process in $(C_8H_{20}N)_2TeCl_6$. (**B**) PXRD patterns of $(C_8H_{20}N)_2TeCl_6$ stored in the atmosphere for 60 d. (**C**) The PL map of $(C_8H_{20}N)_2TeCl_6$ sample under different blue light excitation times.

4. Conclusions

In summary, we successfully synthesized a 0D $(C_8H_{20}N)_2TeCl_6$ single crystal through various methods and investigated the STE mechanism of broadband luminescence. The crystal structure of $(C_8H_{20}N)_2TeCl_6$ was identified in the space group $P2_1/c$ and comprised $[TeCl_6]^{2-}$ octahedral and charge-balancing $C_8H_{20}N^+$ cations. $(C_8H_{20}N)_2TeCl_6$ single crystals exhibited a yellow-orange emission (≈600 nm) with a large FWHM of 130 nm. And it exhibits a unique ultrabroad excitation band containing a blue excitation region. The color purity of $(C_8H_{20}N)_2TeCl_6$ halide is 95.2%. The temperature-dependent optical properties demonstrate that the Huang–Rhys factor and exciton binding energy were 38.71 and 338.27 meV, respectively, indicative of strong electron–phonon coupling. Therefore, we attributed the origin of the yellow-orange emission band to STE emission of $[TeCl_6]^{2-}$ octahedral. Our achievement in $(C_8H_{20}N)_2TeCl_6$ single crystals offers a strategy for designing and synthesizing Pb-free, low-dimensional, luminescent metal halides with broad blue-light excitation.

Supplementary Materials: The following supporting information can be downloaded at https://www.mdpi.com/article/10.3390/nano14010046/s1, Figure S1: Diagram of synthesis of $(C_8H_{20}N)_2TeCl_6$; Figure S2: PXRD patterns of $(C_8H_{20}N)_2TeCl_6$; Figure S3: Scheme of the energy level of $(C_8H_{20}N)_2TeCl_6$ and the $v2$ vibration mode of $[TeCl_6]^{2-}$ octahedra; Figure S4: PLQY of $(C_8H_{20}N)_2TeCl_6$; Tables S1−S7: crystallographic data; Table S8: PL lifetimes of $(C_8H_{20}N)_2TeCl_6$.

Author Contributions: X.Y.: conceptualization, methodology, investigation, data curation, writing—original draft. J.N.: investigation, writing—review and editing. H.H. and H.Z.: writing—review and editing. D.X., Y.S. and H.L.: supervision, investigation, writing—review and editing. All authors have read and agreed to the published version of the manuscript.

Funding: This research was funded by the National Natural Science Foundation of China (Grant No. 61874074), Science and Technology Project of Shenzhen (Grant No. JCYJ20220531100815034), and Guangdong Basic and Applied Basic Research Foundation (General Program, Grant No. 2022A1515012055).

Data Availability Statement: The data presented in this study are available on request from the corresponding author.

Conflicts of Interest: The authors declare no conflict of interests.

References

1. Luo, J.J.; Wang, X.M.; Li, S.R.; Liu, J.; Guo, Y.M.; Niu, G.D.; Yao, L.; Fu, Y.H.; Gao, L.; Dong, Q.S.; et al. Efficient and stable emission of warm-white light from lead-free halide double perovskites. *Nature* **2018**, *563*, 541–545. [CrossRef]
2. Tan, Z.F.; Li, J.H.; Zhang, C.; Li, Z.; Hu, Q.S.; Xiao, Z.W.; Kamiya, T.; Hosono, H.; Niu, G.D.; Lifshitz, E.; et al. Highly efficient blue-emitting Bi-doped Cs_2SnCl_6 perovskite variant: Photoluminescence induced by impurity doping. *Adv. Funct. Mater.* **2018**, *28*, 1801131. [CrossRef]
3. Yan, J.K.; Li, H.J.; Aldamasy, M.H.; Frasca, C.; Abate, A.; Zhao, K.; Hu, Y. Advances in the synthesis of halide perovskite single crystals for optoelectronic applications. *Chem. Mater.* **2023**, *35*, 2683–2712. [CrossRef]

4. Zhang, F.; Zhang, Q.; Liu, X.; Hu, Y.F.; Lou, Z.D.; Hou, Y.B.; Teng, F. Property modulation of two-dimensional lead-free perovskite thin films by aromatic polymer additives for performance enhancement of field-effect transistors. *ACS Appl. Mater. Interfaces* **2021**, *13*, 24272–24284. [CrossRef] [PubMed]
5. Saidaminov, M.I.; Abdelhady, A.L.; Murali, B.; Alarousu, E.; Burlakov, V.M.; Peng, W.; Dursun, I.; Wang, L.F.; He, Y.; Maculan, G.; et al. High-quality bulk hybrid perovskite single crystals within minutes by inverse temperature crystallization. *Nat. Commun.* **2015**, *6*, 7586. [CrossRef] [PubMed]
6. Zhang, C.; Liu, X.L.; Chen, J.; Lin, J. Solution and solid-phase growth of bulk halide perovskite single crystals. *Chin. J. Chem.* **2021**, *39*, 1353–1363. [CrossRef]
7. Yao, J.S.; Wang, J.J.; Yang, J.N.; Yao, H.B. Modulation of metal halide structural units for light emission. *Acc. Chem. Res.* **2021**, *54*, 441–451. [CrossRef] [PubMed]
8. Li, T.S.; Luo, S.L.; Wang, X.J.; Zhang, L.J. Alternative lone-pair ns^2-cation-based semiconductors beyond lead halide perovskites for optoelectronic applications. *Adv. Mater.* **2021**, *33*, 2008574. [CrossRef]
9. McCall, K.M.; Morad, V.; Benin, B.M.; Kovalenko, M.V. Efficient lone-pair-driven luminescence: Structure–property relationships in emissive $5s^2$ metal halides. *ACS Mater. Lett.* **2020**, *2*, 1218–1232. [CrossRef]
10. Huang, T.; Zou, B.S. Luminescent Behavior of Sb^{3+}-Activated Luminescent Metal Halide. *Nanomaterials* **2023**, *13*, 2867. [CrossRef]
11. Fu, Y.P.; Jin, S.; Zhu, X.Y. Stereochemical expression of ns^2 electron pairs in metal halide perovskites. *Nat. Rev. Chem.* **2021**, *5*, 838–852. [CrossRef] [PubMed]
12. Wu, Y.; Li, X.M.; Zeng, H.B. Lead-free halide double perovskites: Structure, luminescence, and applications. *Small Struct.* **2021**, *2*, 2000071. [CrossRef]
13. Zhao, S.Y.; Cai, W.S.; Wang, H.X.; Zang, Z.G.; Chen, J.Z. All-inorganic lead-free perovskite(-like) single crystals: Synthesis, properties, and applications. *Small Methods* **2021**, *5*, 2001308. [CrossRef] [PubMed]
14. Li, S.R.; Luo, J.J.; Liu, J.; Tang, J. Self-trapped excitons in all-inorganic halide perovskites: Fundamentals, status, and potential applications. *J. Phys. Chem. Lett.* **2019**, *10*, 1999–2007. [CrossRef] [PubMed]
15. Nie, J.H.; Zhou, B.; Fang, S.F.; Wang, Y.; Wang, Y.; Tian, B.B.; Hu, H.L.; Zhong, H.Z.; Li, H.N.; Shi, Y.M. Chemical doping of lead-free metal-halide-perovskite related materials for efficient white-light photoluminescence. *Mater. Today Phys.* **2023**, *31*, 100992. [CrossRef]
16. Mao, X.; Wang, Z.Y.; Zhang, F.; Yin, H.; Xu, X.; Chen, J.S.; Chen, Z.; Luo, J.H.; Han, K.L.; Zhang, R.L. All-inorganic zero-dimensional Sb^{3+}-doped $Rb_2ScCl_5(H_2O)$ perovskite single crystals: Efficient self-trapped exciton emission and X-ray detection. *J. Phys. Chem. Lett.* **2023**, *14*, 1521–1527. [CrossRef] [PubMed]
17. Jing, Y.Y.; Liu, Y.; Zhao, J.; Xia, Z.G. Sb^{3+} doping-induced triplet self-trapped excitons emission in lead-free Cs_2SnCl_6 nanocrystals. *J. Phys. Chem. Lett.* **2019**, *10*, 7439–7444. [CrossRef] [PubMed]
18. Yan, S.P.; Liu, S.B.; Teng, Z.W.; Li, H.; Chen, W.Q.; Zhou, W.; Qiu, J.B.; Yu, X.; Wang, S.; Xu, X.H. High quality lead-free perovskites toward white light emitting diodes and X-ray imaging. *J. Mater. Chem. C* **2022**, *10*, 16294–16300. [CrossRef]
19. Li, M.Y.; Lin, J.W.; Wang, N.; Liu, K.J.; Fan, L.B.; Guo, Z.N.; Yuan, W.X.; Zhao, J.; Liu, Q.L. Synthetic-method-dependent antimony bromides and their photoluminescent properties. *Inorg. Chem.* **2022**, *61*, 15016–15022. [CrossRef]
20. Sun, C.; Deng, Z.Y.; Li, Z.Y.; Chen, Z.W.; Zhang, X.Y.; Chen, J.; Lu, H.P.; Canepa, P.; Chen, R.; Mao, L.L. Achieving near-unity photoluminescence quantum yields in organic-inorganic hybrid antimony (III) chlorides with the $[SbCl_5]$ geometry. *Angew. Chem. Int. Ed.* **2023**, *62*, e202216720. [CrossRef]
21. Li, Z.Y.; Li, Y.; Liang, P.; Zhou, T.L.; Wang, L.; Xie, R.J. Dual-band luminescent lead-free antimony chloride halides with near-unity photoluminescence quantum efficiency. *Chem. Mater.* **2019**, *31*, 9363–9371. [CrossRef]
22. Li, M.Z.; Zhou, J.; Molokeev, M.S.; Jiang, X.X.; Lin, Z.S.; Zhao, J.; Xia, Z.G. Lead-free hybrid metal halides with a green-emissive $[MnBr_4]$ unit as a selective turn-on fluorescent sensor for acetone. *Inorg. Chem.* **2019**, *58*, 13464–13470. [CrossRef] [PubMed]
23. Sun, C.; Lu, H.; Yue, C.Y.; Fei, H.H.; Wu, S.F.; Wang, S.H.; Lei, X.W. Multiple light source-excited organic manganese halides for water-jet rewritable luminescent paper and anti-counterfeiting. *ACS Appl. Mater. Interfaces* **2022**, *14*, 56176–56184. [CrossRef] [PubMed]
24. Han, K.; Sakhatskyi, K.; Jin, J.C.; Zhang, Q.Y.; Kovalenko, M.V.; Xia, Z.G. Seed-crystal-induced cold sintering toward metal halide transparent ceramic scintillators. *Adv. Mater.* **2022**, *34*, 2110420. [CrossRef] [PubMed]
25. Zi, L.; Xu, W.; Song, Z.J.; Sun, R.; Liu, S.; Xie, T.Y.; Zhu, J.Y.; Lu, S.Y.; Song, H.W. Highly efficient and stable Cs_2TeCl_6:Cr^{3+} perovskite microcrystals for white light emitting diodes. *J. Mater. Chem. C* **2023**, *11*, 2695–2702. [CrossRef]
26. Liu, R.X.; Zhang, W.J.; Wen, T.Z.; Wen, X.; Ding, C.; Li, Z.F.; Yan, W.B. Excitation-dependent tunable white light of ns^2 ions doped Rb_2SnCl_6 vacancy ordered double perovskite. *J. Phys. Chem. Lett.* **2022**, *13*, 11143–11152. [CrossRef] [PubMed]
27. Wu, L.K.; Sun, H.Y.; Li, L.H.; Li, R.F.; Ye, H.Y.; Li, J.R. Te^{4+}-doping rubidium scandium halide perovskite single crystals enabling optical thermometry. *J. Phys. Chem. C* **2022**, *126*, 21689–21698. [CrossRef]
28. Sedakova, T.V.; Mirochnik, A.G. Structure and luminescent properties of complex compounds of tellurium(IV) with ammonium bases. *Opt. Spectrosc.* **2015**, *119*, 54–58. [CrossRef]
29. Dolomanov, O.V.; Bourhis, L.J.; Gildea, R.J.; Howard, J.A.K.; Puschmann, H. OLEX2: A complete structure solution, refinement and analysis program. *J. Appl. Cryst.* **2009**, *42*, 339–341. [CrossRef]
30. Bourhis, L.J.; Dolomanov, O.V.; Gildea, R.J.; Howard, J.A.K.; Puschmann, H. The anatomy of a comprehensive constrained, restrained refinement program for the modern computing environment—Olex2 dissected. *Acta Cryst.* **2015**, *71*, 59–75.

31. Sheldrick, G.M. A short history of SHELX. *Acta Cryst.* **2008**, *64*, 112–122. [CrossRef] [PubMed]
32. Dai, G.K.; Ma, Z.M.; Qiu, Y.X.; Li, Z.W.; Fu, X.H.; Jiang, H.; Ma, Z.Y. Excitation-dependent luminescence of 0D $((CH_3)_4N)_2ZrCl_6$ across the full visible region. *J. Phys. Chem. Lett.* **2022**, *13*, 7553–7560. [CrossRef]
33. Yan, S.Y.; Tian, W.L.; Chen, H.; Tang, K.X.; Lin, T.T.; Zhong, G.Y.; Qiu, L.Z.; Pan, X.Y.; Wang, W.Z. Synthesis of 0D manganese-based organic–inorganic hybrid perovskite and its application in lead-free red light-emitting diode. *Adv. Funct. Mater.* **2021**, *31*, 2100855. [CrossRef]
34. Peng, H.; Tian, Y.; Zhang, Z.H.; Wang, X.X.; Huang, T.; Dong, T.T.; Xiao, Y.H.; Wang, J.P.; Zou, B.S. Bulk assembly of zero-dimensional organic copper bromide hybrid with bright self-trapped exciton emission and high antiwater stability. *J. Phys. Chem. C* **2021**, *125*, 20014–20021. [CrossRef]
35. Zhou, J.; Rong, X.M.; Molokeev, M.S.; Wang, Y.L.; Yun, X.Y.; Xu, D.H.; Li, X. Alloying Cs^+ into Rb_2ZrCl_6:Te^{4+} toward highly efficient and stable perovskite variant. *Mater. Chem. Front.* **2021**, *5*, 4997–5003. [CrossRef]
36. Liu, Z.X.; Zhou, B.; Fang, S.F.; Nie, J.H.; Zhong, H.Z.; Hu, H.L.; Li, H.N.; Shi, Y.M. Modulation of the excitation states in all-inorganic halide perovskites via Sb^{3+} and Bi^{3+} cooping. *J. Phys. Chem. Lett.* **2023**, *14*, 1022–1028. [CrossRef] [PubMed]
37. Zhang, W.; Zheng, W.; Li, L.Y.; Huang, P.; Gong, Z.L.; Zhou, Z.W.; Sun, J.Y.; Yu, Y.; Chen, X.Y. Dual-Band-Tunable White-Light Emission from Bi^{3+}/Te^{4+} Emitters in Perovskite-Derivative Cs_2SnCl_6 Microcrystals. *Angew. Chem. Int. Ed.* **2022**, *61*, e202116085. [CrossRef]
38. Liu, Y.; Wu, Y.; Juan, Z.L.; Sun, X.; Zhang, W.G.; Zeng, H.B.; Li, X.M. Efficient, Stable, and Tunable Cold/Warm White Light from Lead-Free Halide Double Perovskites $Cs_2Zr_{1-x}Te_xCl_6$. *Adv. Opt. Mater.* **2021**, *9*, 2100815. [CrossRef]
39. Zhou, B.; Liu, Z.X.; Fang, S.F.; Nie, J.H.; Zhong, H.Z.; Hu, H.L.; Li, H.N.; Shi, Y.M. Emission mechanism of self-trapped excitons in Sb^{3+}-doped all-inorganic metal-halide perovskites. *J. Phys. Chem. Lett.* **2022**, *13*, 9140–9147. [CrossRef]
40. Biswas, A.; Bakthavatsalam, R.; Bahadur, V.; Biswas, C.; Mali, B.P.; Raavi, S.S.K.; Gonnade, R.G.; Kundu, J. Lead-free zero dimensional tellurium(IV) chloride-organic hybrid with strong room temperature emission as a luminescent material. *J. Mater. Chem. C* **2021**, *9*, 4351–4358. [CrossRef]
41. Mao, Y.L.; Zhang, J.; Ren, Q.Q.; Molokeev, M.S.; Zhou, G.J.; Zhang, X.M. Unveiling the uncommon blue-excitable broadband yellow emission from self-trapped excitons in a zero-dimensional hybrid tellurium-based double perovskite. *J. Mater. Chem. C* **2022**, *10*, 17638–17645. [CrossRef]
42. Liu, X.X.; Peng, C.D.; Zhang, L.J.; Guo, D.Y.; Pan, Y.X. Te^{4+}-doped zero-dimensional Cs_2ZnCl_4 single crystals for broadband yellow light emission. *J. Mater. Chem. C* **2022**, *10*, 204–209. [CrossRef]
43. Luo, Z.S.; Liu, Y.J.; Liu, Y.L.; Li, C.; Li, Y.W.; Li, Q.; Wei, Y.; Zhang, L.M.; Xu, B.; Chang, X.Y.; et al. Integrated Afterglow and Self-Trapped Exciton Emissions in Hybrid Metal Halides for Anti-Counterfeiting Applications. *Adv. Mater.* **2022**, *34*, 2200607. [CrossRef] [PubMed]
44. Hu, Z.Y.; Nie, K.; Wang, X.Y.; Duan, X.Q.; Zhou, R.R.; Wu, M.Y.; Ma, X.X.; Zhang, X.D.; Wang, L.X.; Mei, L.F.; et al. Facile synthesis strategy for cesium tin halide perovskite crystals toward light emitting devices and anti-counterfeiting flexible fiber. *Nanoscale* **2023**, *15*, 4893–4898. [CrossRef] [PubMed]
45. Meng, X.F.; Wei, Q.L.; Lin, W.C.; Huang, T.; Ge, S.G.; Yu, Z.M.; Zou, B.S. Efficient yellow self-trapped exciton emission in Sb^{3+}-doped $RbCdCl_3$ metal halides. *Inorg. Chem.* **2022**, *61*, 7143–7152. [CrossRef] [PubMed]
46. Su, B.B.; Li, M.Z.; Song, E.H.; Xia, Z.G. Sb^{3+}-doping in cesium zinc halides single crystals enabling high-efficiency near-infrared emission. *Adv. Funct. Mater.* **2021**, *31*, 2105316. [CrossRef]
47. Jin, J.C.; Peng, Y.H.; Xu, Y.T.; Han, K.; Zhang, A.R.; Yang, X.B.; Xia, Z.G. Bright Green Emission from Self-Trapped Excitons Triggered by Sb^{3+} Doping in Rb_4CdCl_6. *Chem. Mater.* **2022**, *34*, 5717–5725. [CrossRef]
48. Tan, Z.F.; Chu, Y.M.; Chen, J.X.; Li, J.H.; Ji, G.Q.; Niu, G.D.; Gao, L.; Xiao, Z.W.; Tang, J. Lead-free perovskite variant solid solutions $Cs_2Sn_{1-x}Te_xCl_6$: Bright luminescence and high anti-water stability. *Adv. Mater.* **2020**, *32*, 2002443. [CrossRef]
49. Peng, H.; Tian, Y.; Wang, X.X.; Dong, T.T.; Yu, Z.M.; Xiao, Y.H.; Zhang, Z.H.; Wang, J.P.; Zou, B.S. Highly efficient broadband green emission of $(TPA)CuCl_2$ single crystals: Understanding the formation of self-trapped states. *J. Phys. Chem. C* **2022**, *126*, 8545–8552. [CrossRef]
50. Dai, Y.R.; Wei, Q.L.; Chang, T.; Zhao, J.L.; Cao, S.; Zou, B.S.; Zeng, R.S. Efficient self-trapped exciton emission in ruddlesden–popper Sb-doped $Cs_3Cd_2Cl_7$ perovskites. *J. Phys. Chem. C* **2022**, *126*, 11238–11245. [CrossRef]